Scilight

Low-Dimensional Materials

https://www.sciltp.com/journals/ldm

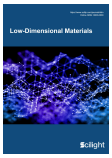

Article

Engineering Oxygen Vacancies and Ion Diffusion Channels via Ni^{2+}/K^{+} Co-Doping for Aqueous Ammonium-Ion Batteries

Xiaoqi Tang [1,†], Nannan Zhong [1,†], Dan Li [2], Jingyi Guan [1], Ning Cao [1], Xiaobei Zang [1,*] and Qingguo Shao [3,*]

[1] Shandong Key Laboratory of Intelligent Energy Materials, School of Materials Science and Engineering, China University of Petroleum (East China), Qingdao 266580, China
[2] Qingdao Fengdong Heat Treatment Co., Ltd., Zhaohong Road, Liuting, Chengyang District, Qingdao 266108, China
[3] Energy Equipment Intelligent Welding Technology Research Center, School of Intelligent Manufacturing and Control Engineering, Shandong Institute of Petroleum and Chemical Technology, Dongying 257061, China
* Correspondence: xiaobeizang@upc.edu.cn (X.Z.); shaoqingguo@sdipct.edu.cn (Q.S.)
† These authors contributed equally to this work.

How To Cite: Tang, X.; Zhong, N.; Li, D.; et al. Engineering Oxygen Vacancies and Ion Diffusion Channels via Ni^{2+}/K^{+} Co-Doping for Aqueous Ammonium-Ion Batteries. *Low-Dimensional Materials* **2025**, *1*(1), 3.

Received: 9 October 2025
Revised: 7 November 2025
Accepted: 10 November 2025
Published: 13 November 2025

Abstract: In ammonium-ion batteries, manganese dioxide (MnO_2) exhibits promising ammonium storage capabilities but suffers from inherent limitations such as poor electrical conductivity and structural instability. To address these challenges, this study proposes a cation doping strategy involving individual (Ni^{2+} or K^{+}) and dual doping strategies. The incorporation of these dopants significantly enhances the ammonium storage performance of MnO_2. Single doping (Ni^{2+} or K^{+}) and dual doping strategies significantly improve the ammonium storage performance of MnO_2. Ni^{2+} doping induces oxygen vacancies and modulates the electronic structure, extending the cycling lifespan to 727 cycles (60% capacity retention) and reducing charge transfer resistance to 9.42 Ω. K^{+} doping forms a KMn_8O_{16} phase with [2 × 2] tunnel structures, elevating the NH_4^{+} diffusion coefficient to 10^{-10}~10^{-9} cm^2 s^{-1} and improving rate capability (73.75 mAh g^{-1} at 1 A g^{-1}). The dual-doped system (NiK-MnO_2) achieves a specific capacity of 165.94 mAh g^{-1} at 0.1 A g^{-1} through synergistic effects. It maintains 60% capacity retention after 917 cycles at 1 A g^{-1} with an impedance of 9.08 Ω and a resistivity of 3.02 mΩ cm. Dual doping improves the electrical conductivity of the electrode material and enhances the ammonium storage performance of MnO_2 through a synergistic mechanism of oxygen vacancies and tunneling structure.

Keywords: ammonium ion batteries; manganese dioxide; doping modification

1. Introduction

Currently, water-based batteries are considered an important research direction in energy storage research due to their high safety, low cost and environmental friendliness [1–3]. Aqueous battery systems include aqueous zinc-ion batteries [4–6], sodium-ion batteries [7,8], magnesium-ion batteries [9,10], etc. These metal-ion batteries show great promise for energy storage applications. However, some systems still face challenges such as dendrite growth, electrolyte corrosion, and limited ion transport kinetics [4,11–14].

Non-metallic ion batteries exhibit potential as alternatives to metal-ion systems due to their distinct electrochemical behavior [15]. Aqueous ammonium ion batteries (AAIBs) can operate under neutral or weakly acidic conditions, which significantly reduces their corrosivity and the occurrence of side reactions [16]. NH_4^{+} has a small hydration ionic radius (3.31 Å) and a low molar mass (18 g mol^{-1}), which contributes to the rapid ionic diffusion of NH_4^{+} in an aqueous solution cell [17]. In addition, the unique tetrahedral molecular structure of NH_4^{+} allows for the formation of hydrogen bonding during intercalation. Hydrogen bonding, which is more flexible than

rigid metal coordination, improves the electrochemical performance of ammonium ion batteries [13]. Recent advances in AAIB cathode materials have demonstrated promising results, including the use of $LiMnO_2$ which achieves stable cycling through hydrogen bonding interactions with NH_4^+ [18], and $LiMn_2O_4$ which provides a stable spinel framework for ammonium ion storage [19]. Therefore, the ammonium ion batteries show a broad application prospect.

The ammonium ion battery is a secondary battery system based on the "rocking chair" mechanism. The principle is that during the charging and discharging process, NH_4^+ reversibly migrates between the cathode and anode electrodes, while electrons are transferred through the external circuit. Since the energy storage of NH_4^+ requires continuous intercalation and deintercalation of the electrode materials, these electrode materials are ideally expected to have a sufficient spatial structure to provide diffusion channels for NH_4^+. Therefore, continued optimization and development of high-performance ammonium ion electrode materials is crucial for advancing ammonium ion batteries. MnO_2 is a promising candidate for NH_4^+ energy storage applications due to its excellent structural properties and high theoretical specific capacity. However, MnO_2 suffers from intrinsically low electronic conductivity, which limits its charge transfer efficiency and rate capability [20]. In addition, in acidic or neutral electrolytes, MnO_2 is prone to Mn^{2+} dissolution, leading to capacity fading [21,22]. While previous studies have explored various Mn-based oxides for ammonium ion storage, the development of doped MnO_2 materials with optimized electronic and ionic transport properties remains largely unexplored.

To address these inherent limitations concurrently, a rational design strategy employing synergistic cationic doping was developed. The selection of Ni^{2+} and K^+ as co-dopants is grounded in their distinct yet complementary functionalities within the MnO_2 lattice. Ni^{2+} incorporation is strategically employed to reinforce the structural integrity of the MnO_2 framework. Its favorable ionic radius and stable valence state effectively mitigate Jahn-Teller distortion while simultaneously inducing oxygen vacancy formation, thereby enhancing bulk electronic conductivity [23,24]. Concurrently, K^+ doping serves as a structural pillar that stabilizes the [2 × 2] tunnel architecture of the resultant KMn_8O_{16} phase [25,26]. This pre-intercalation approach establishes a robust diffusion pathway conducive to rapid NH_4^+ transport while preventing structural collapse during electrochemical cycling.

The present work adopts that the coordinated interaction between these dopant species produces a superior electrode material through a well-defined synergistic mechanism. Specifically, Ni^{2+} induced electronic modulation and structural reinforcement combine with K^+ enabled morphological stabilization to create an optimal environment for concurrent electron and ion transport. This significantly improves the NH_4^+ storage performance of MnO_2, thereby systematically developing high-performance and cost-effective cathode materials for ammonium ion batteries.

2. Experimental

2.1. Materials

All chemicals were used as received. Manganese sulfate monohydrate ($MnSO_4·H_2O$, 99%), ammonium persulfate ($(NH_4)_2S_2O_8$, electrophoretic grade), nickel sulfate hexahydrate ($NiSO_4·6H_2O$, analytically pure), and potassium sulfate (K_2SO_4, 99.99%) were purchased from Shanghai McLean Biochemistry and Technology Co., Ltd. (Shanghai, China) N-methyl pyrrolidone (NMP, chemically pure), polyvinylidene fluoride (PVDF, battery grade), conductive carbon black (ECP-600JD) were purchased from Guangdong Candlelight New Energy Technology Co., Ltd. (Dongguan, China) Stainless steel foil (0.005mm) was purchased from Shenzhen Baide Hardware Machinery Co., Ltd. (Shenzhen, China) Conductive carbon paper (TGP-H-060) was purchased from Toray Industries, Inc. (Tokyo Japan). Glass fiber diaphragm (GF/D) was purchased from Waterman, UK. The rest of the button cell components (CR2032) were purchased from Guangdong Candlelight New Energy Technology Co., Ltd. (Maidstone, UK) Ultrapure water was obtained from the laboratory.

2.2. Synthesis Scheme of NiK-MnO_2 Cathode Materials

0.02 mol of $MnSO_4·H_2O$ was added to 80 mL of deionized water and stirred continuously until $MnSO_4·H_2O$ was completely dissolved. Subsequently, $NiSO_4·6H_2O$ (0.01 mol) and K_2SO_4 (0.005 mol) were added sequentially with magnetic stirring to mix the ions well. Finally, $(NH_4)_2S_2O_8$ (0.02 mol) was added and stirred for one hour. After the stirring was completed, the mixed solution was transferred to the PTFE reactor. The reaction conditions are maintained at 90 °C for 24 h. The solution was centrifuged at a speed of 5000 rpm for 5 min at the end of the reaction for three times, and was then diafiltrated for three times. After the diafiltration was completed, the sample was dried in a vacuum oven at 60 °C for 12 h. The dried solid was ground into black powder named NiK-0.5:0.5. NiK-0.25:0.5, NiK-0.5:0.25, NiK-0.5:1, and NiK-1:0.5 powders were obtained by adjusting the adding amounts

of $NiSO_4 \cdot 6H_2O$ and K_2SO_4. The serial numbers indicate the molar mass ratio of Ni^{2+} to K^+. For comparison, γ-MnO_2, Ni-MnO_2 and K-MnO_2 anode materials were also prepared, and the preparation process is described in SI.

2.3. Characterization of Materials

The structure and composition of materials were analyzed qualitatively and semi-quantitatively using an X-ray diffractometer (XRD, Shimadzu 7000). X-ray photoelectron spectroscopy (XPS, Thermo Scientific K-Alpha) was used to obtain the elemental composition, valence and content of the samples. The surface morphology of the materials was observed by scanning electron microscopy (SEM, TESCAN MIRA LMS), and the internal structure, lattice fringing, and elemental distribution of the samples were observed by transmission electron microscopy (TEM, JEOL JEM-2100F).

2.4. Electrochemical Characterization

The positive electrode sheet was prepared as follows. The active substance (60%), conductive carbon black (30%) and polyvinylidene fluoride (PVDF, 10%) were magnetically stirred in N-methyl-2-pyrrolidone (NMP) solvent for 4 h to obtain a homogeneous slurry. The slurry was then scraped and coated on the surface of stainless-steel foil, and vacuum dried at 60 °C for 12 h to obtain the cathode electrode sheet. The mass loading of the active material on the cathode electrodes is approximately 1.0 mg cm^{-2}. The active material of anode electrode was Perylene-3,4,9,10-tetracarboxylic diimide (PTCDI). The PTCDI was mixed with conductive carbon black and PVDF at a ratio of 8:1:1 to form a uniform slurry, which was then coated onto conductive carbon paper and dried at 60 °C for 12 h to produce the anode electrode pole piece. The obtained 12 mm diameter positive pole pieces and anode pole pieces were assembled with 1 M $(NH_4)_2SO_4$ electrolyte to form a full cell for electrochemical performance testing. The cyclic voltammetry (CV) test voltage interval was 0–1.4 V. The experimental test frequency of AC impedance test (EIS) ranged from 0.01 Hz to 100 kHz with an amplitude of 5 mV, and the Tafel polarization curve test measured a voltage interval of −0.4–0.4 V with a scanning speed of 5 mV s^{-1}. The above tests were performed on an electrochemical workstation CHI760E. The constant current intermittent titration technique (GITT) and constant current charge/discharge (GCD) tests were performed on a Neware test system. All tests were performed at room temperature.

3. Results and Discussion

3.1. Characterization of NiK-MnO_2 Cathode Materials

The crystal structure of NiK-MnO_2 synthesized via an *in situ* reaction was characterized using XRD. As shown in Figure 1a, the diffraction peaks at 2θ = 22.43°, 34.47°, 37.12°, 42.61°, and 56.13° correspond to the (120), (031), (131), (300), and (160) crystallographic planes of γ-MnO_2 (PDF#14-0644). The diffraction peaks at 2θ=12.75°, 18.06°, 28.74°, 47.18°, 49.90° and 60.24° respectively correspond to the (110), (200), (310), (510), (411) and (521) crystal planes of KMn_8O_{16} (PDF#29-1020). These results suggest the coexistence of γ-MnO_2 and KMn_8O_{16} phases. In the KMn_8O_{16} phase, K^+ occupies the interstitial sites within the [2 × 2] tunnels to stabilize the tunnel framework; while in the γ-MnO_2 phase region, Ni^{2+} replaces the Mn sites within the [MnO_6] octahedra. This composite structure of γ-MnO_2 and KMn_8O_{16} is believed to be conducive to combining the good initial structure of the former with the stable [2 × 2] tunnel of the latter, jointly optimizing the storage behavior of NH_4^+.The formation of this composite structure containing both γ-MnO_2 and KMn_8O_{16} phases may originate from the gradient diffusion of K^+ during the synthesis process. Higher concentrations of K^+ in the surface region lead to the preferential formation of the KMn_8O_{16} phase. However, some regions still partially retain the [1 × 2] tunneling structure of pristine γ-MnO_2 due to the limited diffusion kinetics of K^+. These internal γ-MnO_2 regions provide sites for the substitution of Ni^{2+} into the Mn ions within the [MnO_6] octahedra. In the KMn_8O_{16} crystal structure, each K^+ ion is coordinated by eight O^{2-} atoms, forming a distorted body-centered cubic geometric configuration. The average Mn valence in this phase is 3.88+, as determined by the charge balance of the KMn_8O_{16} stoichiometry [24]. The lattice consists of 16 unequal $Mn^{3.88+}$ sites, each coordinated to six O^{2-} ions, forming edge- or corner-sharing [MnO_6] octahedra. These octahedra build up extended tunnel frames by sharing edges or top corners. Figure 1b displays the full XPS spectrum of NiK-MnO_2, confirming the presence of Mn, O, Ni, and K on the material surface. Weak signals of S and N are also observed at their characteristic positions, likely originating from precursor residues [27]. However, the pristine γ-MnO_2 (also containing these residues) shows inferior performance, underscoring that the significant enhancement in NiK-MnO_2 is primarily due to the synergistic effects of Ni^{2+}/K^+ co-doping. Figure 1c shows the elemental mapping, which is consistent with the XPS analysis. The results indicate that Ni^{2+} and K^+ have been

successfully introduced into MnO_2. Figure 1d provides schematic diagrams of the structures of γ-MnO_2, KMn_8O_{16} and NiK-MnO_2, clearly indicating the distinct doping sites of Ni^{2+} and K^+ respectively.

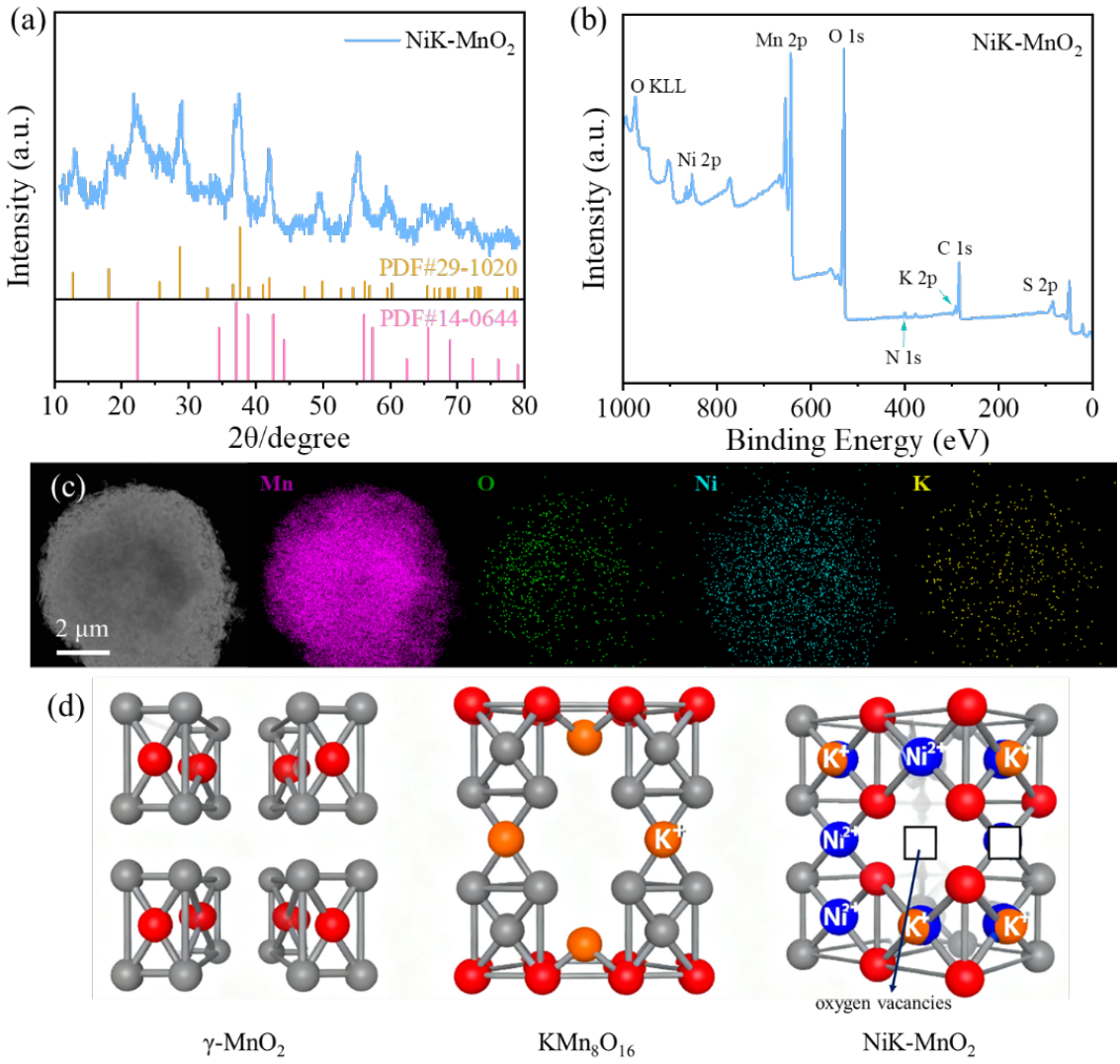

Figure 1. NiK-MnO_2 cathode material (**a**) XRD pattern; (**b**) XPS Survey scan; (**c**) TEM elemental mapping images, (**d**) the structure of γ-MnO_2, KMn_8O_{16}, and NiK-MnO_2.

Microscopic morphological observations reveal that Ni^{2+} and K^+ doping exert distinct effects on the structure of γ-MnO_2. The pristine γ-MnO_2 displays a characteristic needle-like morphology. After Ni ion incorporation, numerous nanosized particles are formed and homogeneously anchored onto the surface of the needle-like matrix (Figure 2b), indicating a particle-decoration effect. In contrast, K^+ doping markedly modifies the needle-like architecture by reducing its diameter and yielding a more compact and densely distributed structure. Notably, the morphology of the Ni/K co-doped sample closely resembles that of the K-MnO_2, suggesting that K ions play a dominant role in determining the final morphological characteristics. To further elucidate the structural evolution induced by ion doping, high-resolution TEM analysis was conducted. The lattice spacing of 0.291 nm observed in the Ni-MnO_2 sample corresponds to the (031) plane of γ-MnO_2 (Figure 2f). In the K-MnO_2 sample, lattice spacings of 0.496 nm and 0.242 nm are assigned to the (200) plane of the KMn_8O_{16} phase and the (131) plane of the γ-MnO_2 phase, respectively (Figure 2g). For the NiK-MnO_2 sample, lattice spacings of 0.311 nm and 0.164 nm are indexed to the (310) plane of KMn_8O_{16} and the (160) plane of γ-MnO_2, respectively. These results indicate the coexistence of γ-MnO_2 and KMn_8O_{16} phases in both K-MnO_2 and NiK-MnO_2, further confirming that the introduction of K ions induces the formation of the KMn_8O_{16} phase.

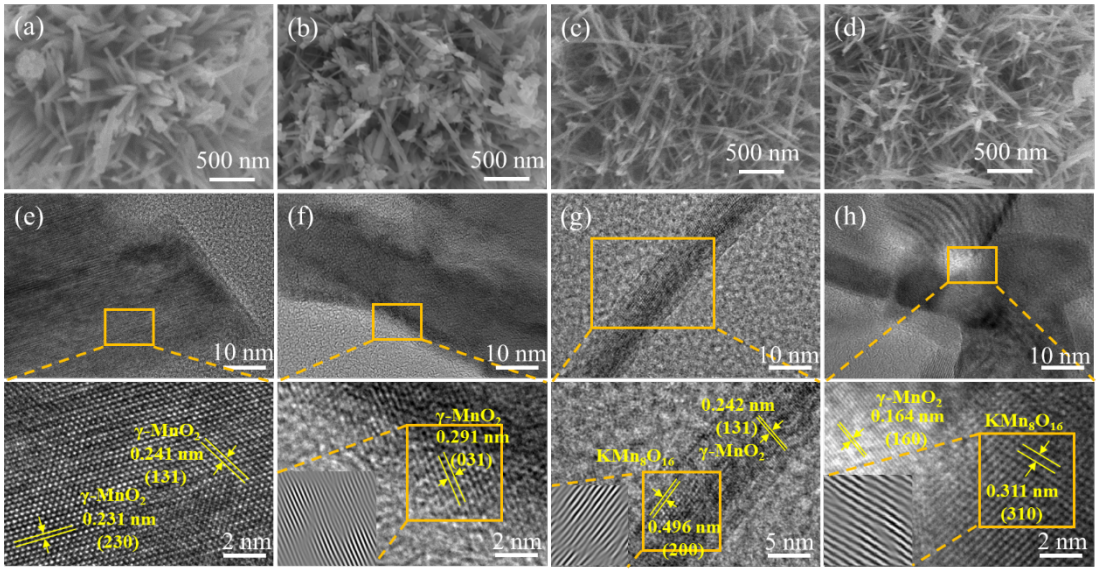

Figure 2. SEM images of (**a**) γ-MnO_2; (**b**) Ni-MnO_2; (**c**) K-MnO_2 and (**d**) NiK-MnO_2; TEM images of (**e**) γ-MnO_2; (**f**) Ni-MnO_2; (**g**) K-MnO_2 and (**h**) NiK-MnO_2.

3.2. Electrochemical Properties

To evaluate the electrochemical applicability of the electrode materials, full cells were assembled using NiK-MnO_2 as the cathode and PTCDI as the anode. Figure 3a presents the GCD curves of NiK-MnO_2 with different Ni/K molar ratios in comparison to pristine γ-MnO_2. The GCD profiles and rate performance of pristine γ-MnO_2 synthesized under various conditions are provided in Figure S2. Compared with undoped γ-MnO_2, all NiK-MnO_2 samples exhibit significantly enhanced specific capacities across different doping ratios. The rate performance comparison (Figure 3b) further demonstrates that NiK-MnO_2 delivers higher capacities than γ-MnO_2 at all current densities. The cycling performance at 1 A g^{-1} is illustrated in Figure 3c, where the NiK-0.5:0.5 sample delivers a higher initial capacity and maintains approximately 60% of its capacity after 917 cycles, while pristine γ-MnO_2 suffers from both lower initial capacity and inferior cycling stability. These results highlight that Ni^{2+}/K^+ co-doping effectively mitigates capacity fading, underscoring its potential advantages in electrode material design. A detailed rate performance evaluation of NiK-MnO_2 was further conducted. As shown in Figure 3d, the NiK-0.5:0.5 sample delivers specific capacities of 165.94, 162.20, 145.83, 127.27, and 113.28 mAh g^{-1} at current densities of 0.1, 0.2, 0.5, 0.8, and 1.0 A g^{-1}, respectively. When the current density returns to 0.1 A g^{-1}, the capacity recovers to 169.92 mAh g^{-1}, corresponding to a retention rate exceeding 100% (Figure 3e), demonstrating excellent reversibility and rate capability.

To further investigate the effects of Ni^{2+} and K^+ on the battery performance in the NiK-MnO_2 dual-ion doping system, single-ion doped Ni-MnO_2 and K-MnO_2 cathode materials were also prepared respectively (the comparison of electrochemical performance of single-ion doping ratio is shown in Figure S3). The samples exhibiting optimal electrochemical performance of Ni-MnO_2 and K-MnO_2 cathode materials were selected for comparison with the double-ion doped samples respectively. As shown in Figure 4a, the specific capacity of the Ni-MnO_2 cathode material increases significantly from 92.01 mAh g^{-1} (undoped γ-MnO_2) to 182.67 mAh g^{-1} at a current density of 0.1 A g^{-1}. However, at a higher current density of 1 A g^{-1}, its specific capacity drops to 74.91 mAh g^{-1}, indicating limited rate capability. As illustrated in Figure 4c, the cycling performance of various cathode materials is demonstrated at a current density of 1 A g^{-1}. The introduction of Ni^{2+} into γ-MnO_2 causes moderate lattice distortion, which helps maintain structural integrity during cycling. This is consistent with reports that Ni^{2+} doping can suppress Jahn-Teller distortion of Mn^{3+} and reinforce the MnO_2 framework, thereby mitigating structural degradation during cycling [28]. Furthermore, transition metal dopants like Ni^{2+} are known to act as structural pillars, enhancing the stability of MnO_2 tunnel structures during ion insertion/extraction [29]. As a result, the Ni-MnO_2 cathode can retain 60% of its initial capacity after 691 cycles, significantly outperforming the 253 cycles of undoped γ-MnO_2. The doping of Ni^{2+} significantly improved the specific capacity of γ-MnO_2 at small current density and the cycling stability at high current density, but it did not significantly improve the rate capacity of the battery. The specific capacities of K-MnO_2 full cells at current densities of 0.1, 0.2, 0.5, 0.8 and 1.0 A g^{-1} are 175.83, 164.90, 135.28, 109.85 and 95.21 mAh g^{-1} respectively (Figure 4a). In comparison with Ni-MnO_2 and γ-MnO_2 cathode materials, K-MnO_2 cathode materials demonstrate superior specific capacity and rate

capacity. However, at 1A g^{-1} current density, when the remaining capacity of the full cell assembled from K-MnO_2 was 60% (Figure 4c), the number of cycling turns of K-MnO_2 cathode material was 412, and the cycling performance was slightly lower than that of Ni-MnO_2 cathode material. Although K^+ insertion into the tunnels of KMn_8O_{16} enhances structural stability and mitigates collapse during cycling, its effect is weaker than the structural stabilization provided by Ni^{2+}. It is important to note that these incorporated K^+ ions function as stable pillars within the [2 × 2] tunnels and are not extracted during cycling; their primary role is to pre-stabilize the diffusion channels for NH_4^+, rather than to participate in the electrochemical reaction. The superior stabilization from Ni^{2+} is attributed to its stronger bonding with the oxygen framework, which not only provides a pillar effect but also directly strengthens the covalent bonding within the MnO_6 octahedra, leading to a more robust structure against repeated cycling [30,31]. The Ni/K double-doped γ-MnO_2 system exhibits significantly superior electrochemical rate capacity and cycling stability in comparison to the single-doped system. The enhancement in performance is primarily attributed to the synergistic stabilizing effect of Ni^{2+} and K^+ in modulating the lattice frameworks and suppressing structural distortions [24].

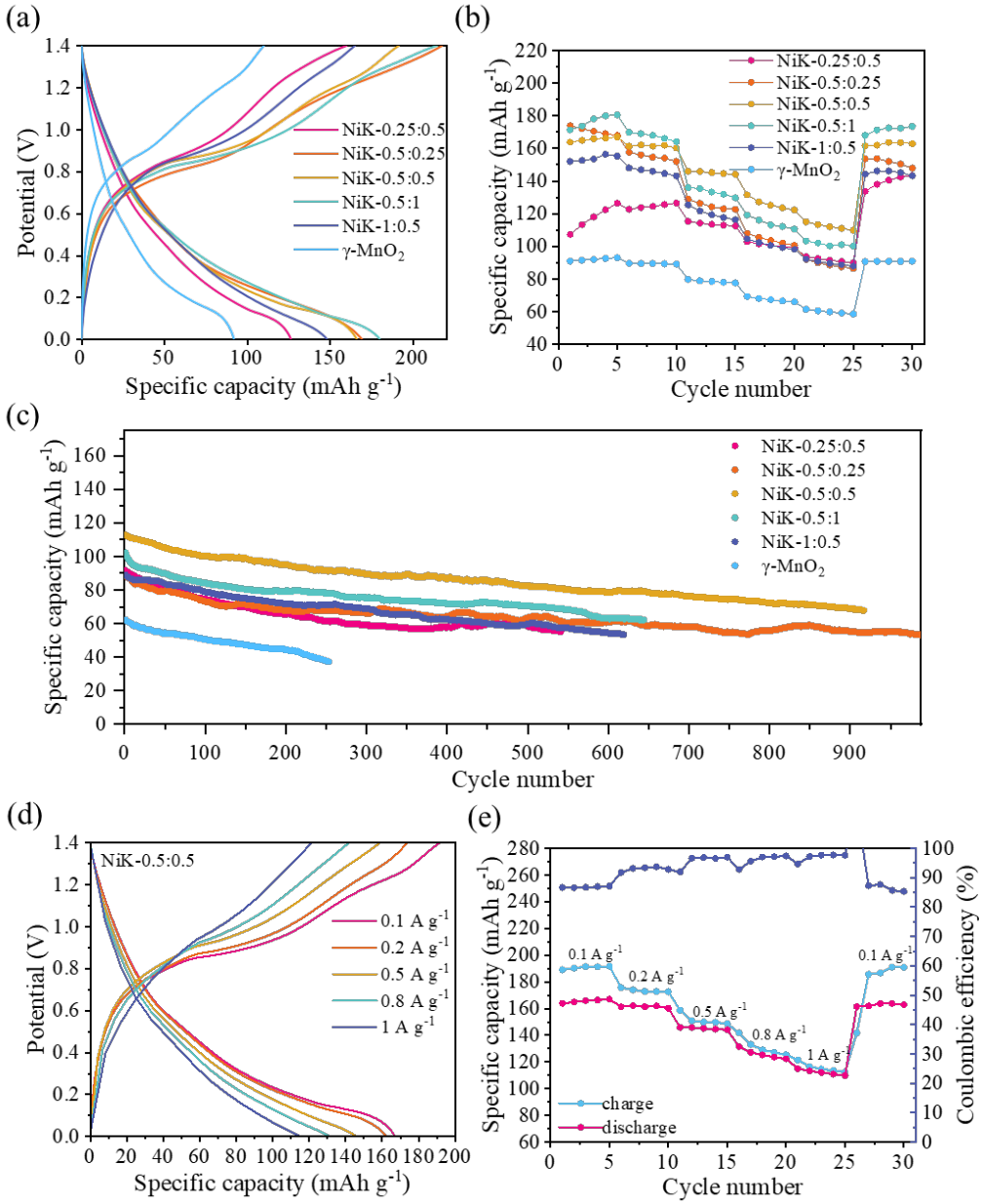

Figure 3. GCD curves of NiK-MnO_2 and γ-MnO_2 at different proportions (**a**) 0.1A g^{-1}; (**b**) Magnification performance graph; (**c**) Cyclic curve at 1 A g^{-1}. NiK-0.5:0.5 cathode material (**d**) GCD curves at different current densities; (**e**) Magnification performance graph.

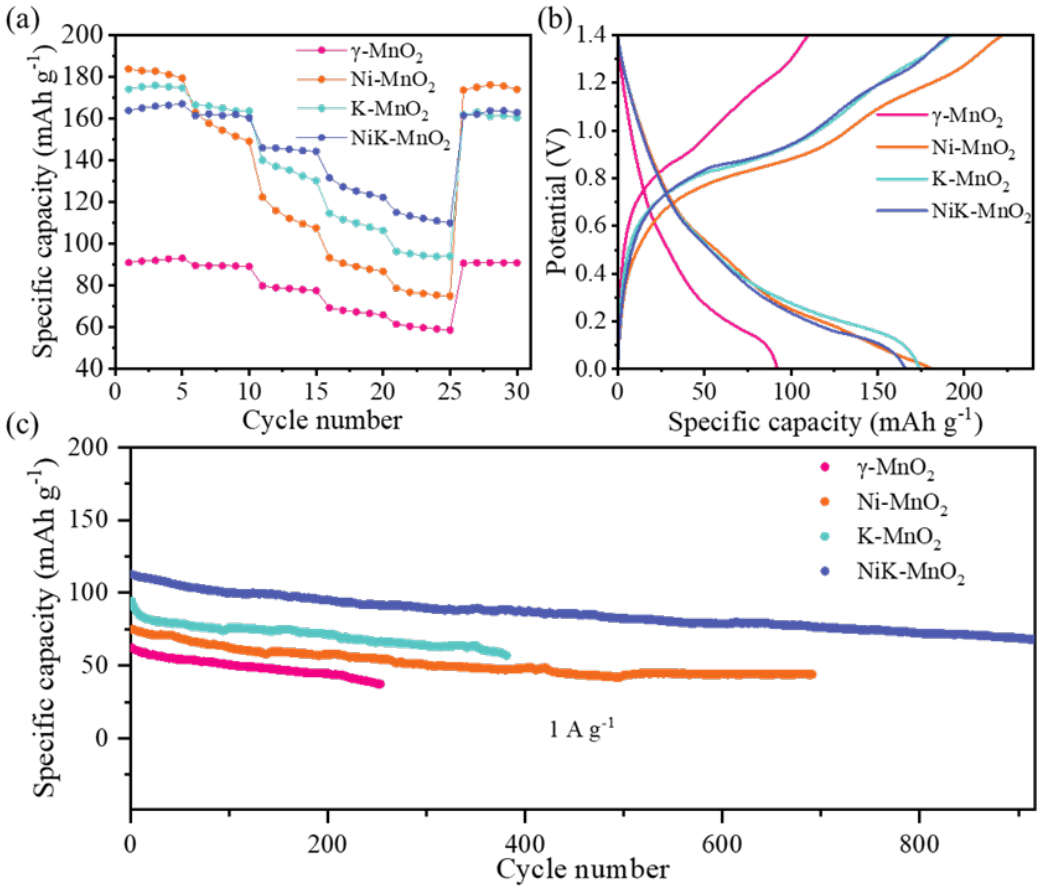

Figure 4. γ-MnO_2, Ni-MnO_2, K-MnO_2, NiK-MnO_2 cathode materials (**a**) rate capacity plot; (**b**) first turn GCD plot; (**c**) cycling performance plot.

In order to further explore the mechanism of metal ions in MnO_2, XPS analysis was conducted to examine the variation in oxidation states for γ-MnO_2, Ni-MnO_2, K-MnO_2, and NiK-MnO_2. Figure 5a shows the high-resolution O 1s spectrum, which is deconvoluted into three distinct peaks. The binding energies of these three peaks are 529.63 eV, 531.2 eV, and 532.76 eV, which are attributed to lattice oxygen (O_{lat}), adsorbed oxygen (O_{ads}), and surface hydroxyl groups (O_{O-H}) respectively [32]. Since O_{ads} is typically adsorbed at oxygen vacancies, its concentration can indirectly reflect the oxygen vacancy content [33]. The presence of oxygen vacancies exposes more active sites, thus providing significant advantages in electrochemical reactions. However, excessive oxygen vacancies may lead to structural instability and reduce the cycle life. The incorporation of Ni^{2+} or K^+ into γ-MnO_2 leads to a charge imbalance. This imbalance can be neutralized by the formation of oxygen vacancies, which helps maintain charge neutrality and stabilize the crystal structure. In Ni-MnO_2, the O_{ads}/O_{lat} ratio increases to 0.42, compared to 0.38 in undoped γ-MnO_2. The O_{ads}/O_{lat} ratio of K-MnO_2 is even higher, reaching 0.52. However, the excessive oxygen vacancies in K-MnO_2 compromise its cycling stability. In NiK-MnO_2, the O_{ads}/O_{lat} ratio is 0.47, suggesting that co-doping provides a balance between maintaining structural integrity and offering sufficient active sites. To further validate the effectiveness of oxygen vacancy regulation, XPS analysis was performed to investigate the valence state distribution of Mn. As illustrated in Figure 5b, the high-resolution Mn 2p spectrum reveals the presence of spin-orbit splitting peaks for both the Mn $2p_{3/2}$ and Mn $2p_{1/2}$ states. These peaks correspond to binding energies of 641.46 eV and 653.16 eV, respectively, with an overall spin-orbit splitting energy of 11.7 eV. Furthermore, peaks with binding energies of 642.02 eV and 653.69 eV can be attributed to Mn^{3+}, while those with binding energies of 643.95 eV and 655.67 eV correspond to Mn^{4+}. The Mn^{3+}/Mn^{4+} ratios for Ni-MnO_2, K-MnO_2, and NiK-MnO_2 are 0.54, 0.89, and 0.61, respectively, higher than that of undoped γ-MnO_2 (0.41). This result confirms that both Ni^{2+} and K^+ can effectively modulate the local electronic environment, change the charge distribution, and promote the formation of oxygen vacancies. In the dual-ion doped NiK-MnO_2 system, the combination of Ni^{2+} induced structural stability and K^+ induced lattice modulation leads to a uniform distribution of oxygen vacancies and a robust local environment, ensuring efficient ion transport and cycling stability.

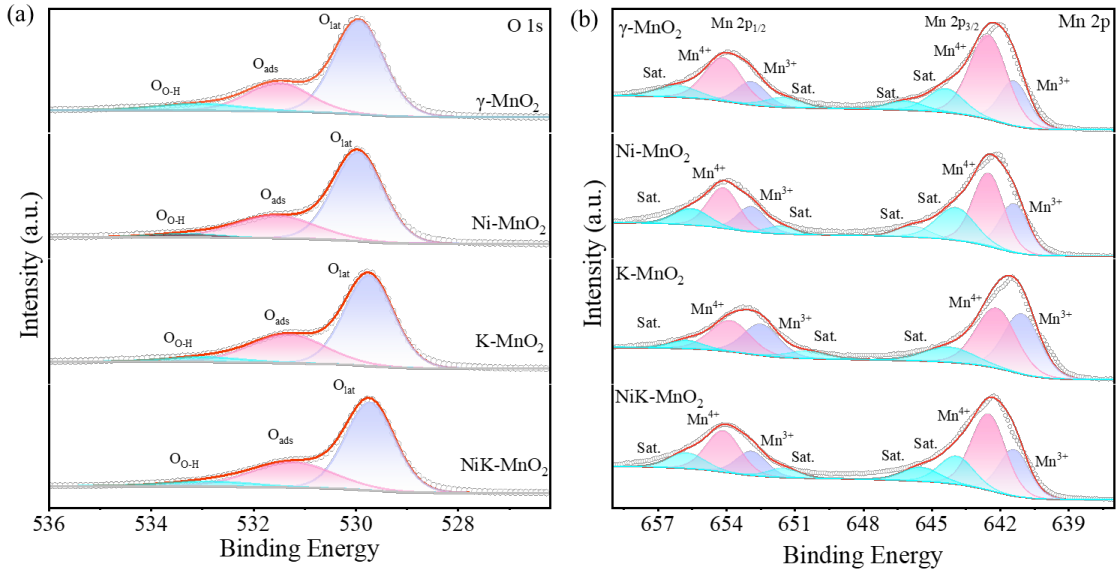

Figure 5. High-resolution spectrum of γ-MnO_2, Ni-MnO_2, K-MnO_2, and NiK-MnO_2 cathode materials (**a**) O 1s; (**b**) Mn 2p.

Cyclic voltammetry curves of NiK-MnO_2 were measured at various scan rates (0.1–1.0 mV s^{-1}) to investigate its electrochemical kinetics. By analyzing the dependence of current response on scan rate, cv curve provides insight into whether the charge-storage process is dominated by pseudocapacitive contributions or diffusion-controlled mechanisms, elucidating the intrinsic reaction kinetics of the electrode. The cv curves exhibit two oxidation peaks and two reduction peaks, with their potentials at 0.9, 1.3, 0.1, and 0.5 V, respectively. The curves maintain their shape with increasing scan rate, indicating stable electrochemical behavior. Figure 6b presents the log-log plot of peak current versus scan rate, along with the corresponding linear fitting curve. The calculation formula is [34]:

$$i = av^b$$

$$\log i = b\log v + \log a$$

From this formula, the b values corresponding to the four redox peaks are 0.75, 0.77, 0.96 and 0.98 respectively, indicating the coexistence of both diffusion-controlled and pseudocapacitive-controlled charge storage mechanisms. The contribution of the diffusion-controlled process and pseudocapacitive-controlled process to the total current i was calculated by the following equation [35]:

$$i = k_1 v + k_2 v^{\frac{1}{2}}$$

Figure 6c shows the pseudocapacitive contribution of 85.54% at a sweep speed of 1 mV s^{-1}. Figure 6d demonstrates the pseudocapacitive contribution at different sweep speeds, which is 62.93%, 74.23%, 82.37%, and 82.75% at sweep speeds of 0.1, 0.2, 0.5, and 0.8 mV s^{-1} respectively. This scan-rate-dependent behavior reveals a mixed charge-storage mechanism. At a slower, more practical scan rate of 0.1 mV s^{-1}, the diffusion-controlled process still contributes significantly (~37.07%), indicating that both diffusion and capacitive processes are involved. As the scanning rate increases, the proportion of the pseudocapacitive contribution rises markedly. This indicates that during rapid charging and discharging, the electrochemical reaction kinetics are increasingly dominated by the surface-controlled pseudocapacitive behavior, while the overall mechanism remains a combination of both processes.

In order to investigate the effect of Ni^{2+}/K^+ co-doping on the diffusion coefficient of ammonium ions, a series of GITT tests were conducted on a range of cathode materials. Based on the formula:

$$D_{NH_4^+} = \frac{4}{\pi\tau}\left(\frac{mV_m}{MS}\right)^2\left(\frac{\Delta E_S}{\Delta E_\tau}\right)^2$$

The ammonium ion diffusion coefficients of Ni-MnO_2 were calculated to be in the order of magnitude between 10^{-12} and 10^{-10} cm^2 s^{-1} (Figure S4a), which is of the same order of magnitude (10^{-12} to 10^{-10} cm^2 s^{-1}) as that of the undoped sample γ-MnO_2 (Figure S4b). This indicates that Ni^{2+} doping failed to effectively increase the migration rate of ammonium ions in the electrode materials. Due to the limitation of the diffusion coefficient of

ammonium ions, the amount of ion migration under high-current conditions could not meet the demand of rapid electrochemical reactions. This led to an increase in the concentration gradient within the material and exacerbates the polarization phenomenon. Consequently, the rate performance of the Ni-MnO_2 electrode was not significantly improved. The ammonium ion diffusion coefficients of K-MnO_2 were in the range of 10^{-10}~10^{-9} cm^2 s^{-1} (Figure S4c), with an enhancement of diffusion coefficients by two orders of magnitude. This phenomenon is attributed to the fact that the suitable K^+ addition optimizes the internal structure of the material and forms a more ideal ammonium ion diffusion channel. The distribution of K^+ in the tunneling basically does not interfere with the diffusion of ammonium ions, which can move rapidly through the electrode material, which explains the substantial improvement in the rate performance of K-MnO_2. The ammonium-ion diffusion coefficient of NiK-MnO_2 is stably distributed within the range of 10^{-10}–10^{-9} cm^2 s^{-1} (Figure 7a), maintaining the same order of magnitude as K-MnO_2. This result confirms the excellent rate performance of NiK-MnO_2. Further analysis of the interfacial charge-transfer characteristics of different cathode materials was conducted using electrochemical impedance spectroscopy (Figure 7b). The charge-transfer resistance (Rct) of γ-MnO_2 is 22.74 Ω, while that of Ni-MnO_2 and K-MnO_2 is 10.13 Ω and 17.89 Ω, respectively. The reduction in Rct upon Ni or K doping can be attributed to the significant increase in oxygen vacancy concentration and the enhanced electronic conductivity induced by the multivalence states of manganese. For NiK-MnO_2, Rct further decreases to 8.08 Ω, indicating optimal interfacial charge-transfer efficiency. The synergistic effect of dual-ion doping promotes simultaneous enhancement of electron and ion transport, thereby significantly improving the overall conductivity of MnO_2. Meanwhile, Tafel polarization curves measured in a three-electrode system (Figure 7c) reveal that NiK-MnO_2 exhibits a corrosion current density (i_{corr}) of 0.018 mA cm^{-2}, much lower than that of the other samples. This indicates a lower self-corrosion rate and higher chemical stability in the electrolyte, further confirming the stabilizing effect of Ni^{2+}/K^+ co-doping. Compared with previously reported cathode materials (Figure 7d), it is demonstrated that the NiK-MnO_2 prepared in this work possesses higher specific capacity and superior rate performance.

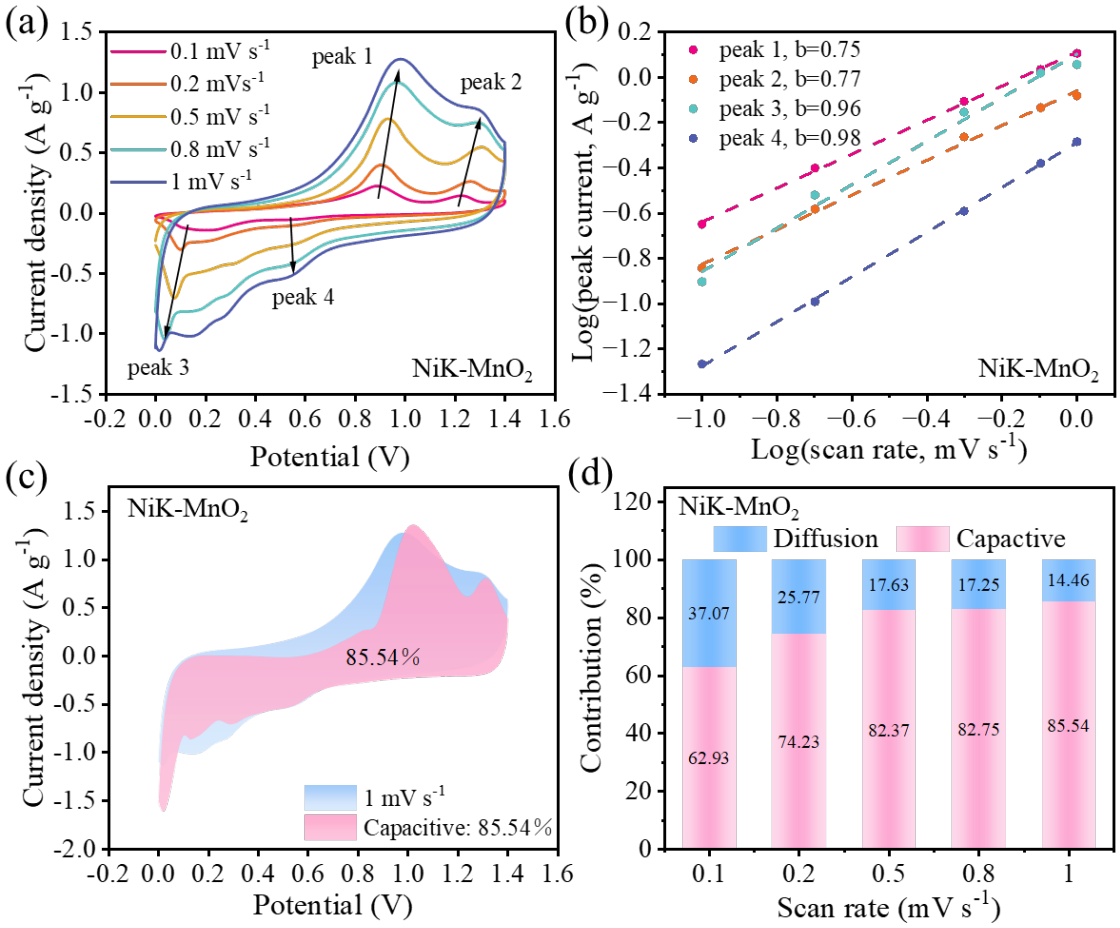

Figure 6. NiK-MnO_2 (**a**) CV curves at different sweep rates; (**b**) logi and logv plots of redox peaks; (**c**) pseudocapacitive and diffusion-controlled contributions at 1 mV s^{-1}; (**d**) pseudocapacitive and diffusion-controlled contributions at various scan rates.

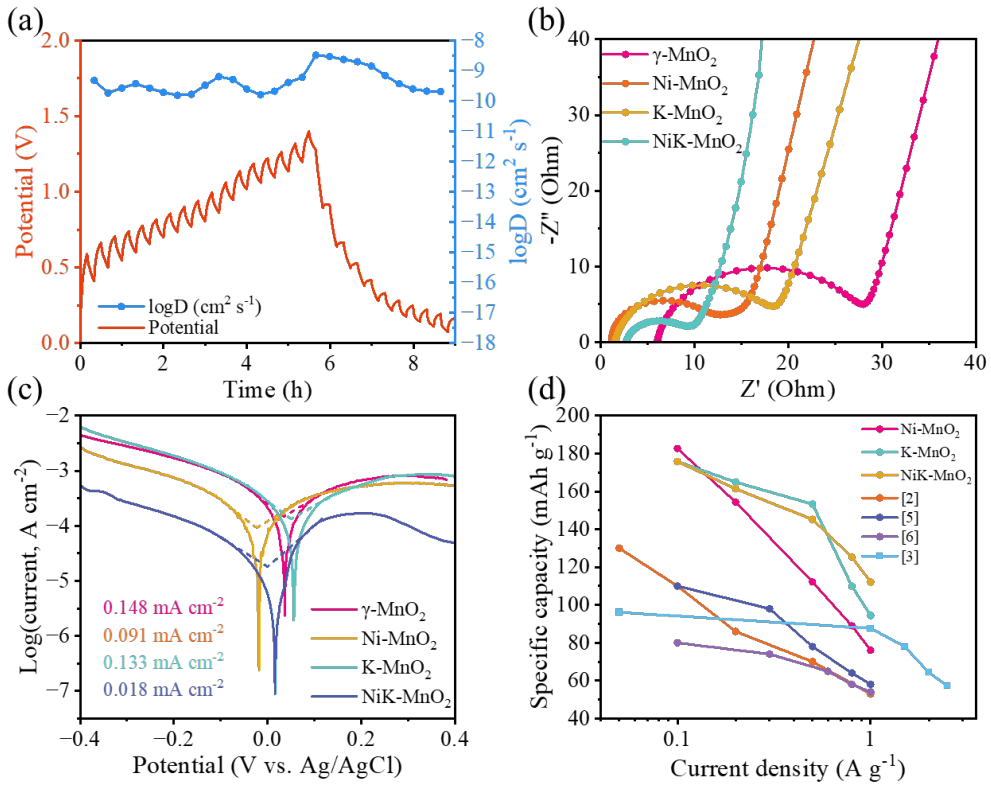

Figure 7. (**a**) GCD curves and corresponding diffusion coefficients in the GITT test of NiK-MnO_2; γ-MnO_2, Ni-MnO_2, K-MnO_2, NiK-MnO_2 of (**b**) EIS curves; (**c**) Tafel polarization curves; (**d**) Comparison of the specific capacity of Ni-MnO_2, K-MnO_2, NiK-MnO_2 and existing cathode materials.

4. Conclusions

In summary, NiK-MnO_2 cathode materials were prepared by *in situ* synthesis, where Ni^{2+} doping significantly enhanced the conductivity of the materials through oxygen vacancy induction, while K^+ doping promoted ion diffusion through a stable tunneling structure. The co-doping of Ni^{2+} with K^+ has been shown to break through the performance limitations of single doping through the synergistic effect of the oxygen vacancy-tunnelling structure. The electrochemical performance of the battery was optimal when Ni:K=0.5:0.5. At this ratio, the material exhibited excellent rate capability and cycling stability. The specific capacity at 1 A g^{-1} current density was 113.28 mAh g^{-1}, and the capacity remained 60% after 917 cycles. Therefore, the successful synthesis of NiK-MnO_2 cathodes provides a promising strategy for developing aqueous ammonium-ion batteries with prolonged cycling stability, improved capacity, and superior rate performance.

Supplementary Materials

The additional data and information can be downloaded at: https://media.sciltp.com/articles/others/251113144210180 5/LDM-25100032-Supplementary-Materials-FC-done.pdf. Figure S1: XRD diffraction patterns of γ-MnO_2, Ni-MnO_2 and K-MnO_2. Figure S2: γ-MnO_2 with different synthesis temperatures (**a**) GCD curves; (**b**) rate performance curves; γ-MnO_2 with different $(NH_4)_2S_2O_8$ additions (**c**) GCD curves; (**d**) multiplicity performance curves. Figure S3: GCD curves for different ratios of Ni-MnO_2 at (**a**) 0.1 A g^{-1}; (**b**) plots of multiplicative performance; (**c**) cycling curves at 1 A g^{-1}; GCD curves for different ratios of K-MnO_2 at (**a**) 0.1 A g^{-1}; (**b**) plots of multiplicative performance; (**c**) cycling curves at 1 A g^{-1}. Figure S4: (**a**) GCD curves and corresponding diffusion coefficients in γ-MnO_2 GITT test, (**b**) GCD curves and corresponding diffusion coefficients in Ni-MnO_2 GITT test; (**c**) GCD curves and corresponding diffusion coefficients in K-MnO_2 GITT test.

Author Contributions

X.T.: writing—original draft, formal analysis, data curation. N.Z.: writing—original draft, formal analysis, data curation. D.L.: validation, data curation. J.G.: writing—review & editing. N.C.: writing—review & editing, supervision, resources, funding acquisition. X.Z.: writing—review & editing, methodology, data curation, project administration. Q.S.: writing—review & editing, methodology, funding acquisition. All authors have read and agreed to the published version of the manuscript.

Funding

This work was supported by the China University of Petroleum (East China) Independent Innovation Research Program for Youth Fund (27RA2408006), China University of Petroleum (East China) College Students' Innovation and Entrepreneurship Training Program (202506071CX), Shandong Provincial Natural Science Foundation (ZR2025MS938), and Taishan Scholars Program of Shandong Province (No. tsqn202507273).

Institutional Review Board Statement

Not applicable.

Informed Consent Statement

Not applicable.

Data Availability Statement

Not applicable.

Conflicts of Interest

The authors declare no conflict of interest.

Use of AI and AI-Assisted Technologies

No AI tools were utilized for this paper.

References

1. Han, J.; Varzi, A.; Passerini, S. The emergence of aqueous ammonium-ion batteries. *Angew. Chem.* **2022**, *134*, e202115046.
2. Pan, Y.; Yuan, L.; Liu, L.; et al. Critical advances of aqueous rechargeable ammonium ion batteries. *Small Struct.* **2023**, *4*, 2300201.
3. Zhang, R.; Wang, S.; Chou, S.; et al. Research development on aqueous ammonium-ion batteries. *Adv. Funct. Mater.* **2022**, *32*, 2112179.
4. Ao, H.; Zhu, W.; Liu, M.; et al. High-Voltage and Super-Stable Aqueous Sodium–Zinc Hybrid Ion Batteries Enabled by Double Solvation Structures in Concentrated Electrolyte. *Small Methods* **2021**, *5*, 2100418.
5. Zhang, Q.; Luan, J.; Tang, Y.; et al. Interfacial design of dendrite-free zinc anodes for aqueous zinc-ion batteries. *Angew. Chem. Int. Ed.* **2020**, *59*, 13180–13191.
6. Hu, F.; Xie, D.; Zhao, D.; et al. $Na_2V_6O_{16}\cdot 2.14H_2O$ nanobelts as a stable cathode for aqueous zinc-ion batteries with long-term cycling performance. *J. Energy Chem.* **2019**, *38*, 185–191.
7. Zeng, Y.; Yang, J.; Yang, H.; et al. Bridging microstructure and sodium-ion storage mechanism in hard carbon for sodium ion batteries. *ACS Energy Lett.* **2024**, *9*, 1184–1191.
8. Wang, Q.; Zhou, D.; Zhao, C.; et al. Fast-charge high-voltage layered cathodes for sodium-ion batteries. *Nat. Sustain.* **2024**, *7*, 338–347.
9. Sun, T.; Yao, X.; Luo, Y.; et al. Micron-sized $Na_{0.7}MnO_{2.05}$ as cathode materials for aqueous rechargeable magnesium-ion batteries. *Ionics* **2019**, *25*, 4805–4815.
10. You, H.; Yang, C.; Liu, Z.; et al. Heterojunction of Vanadium Oxide Nanobelts for Aqueous Magnesium-Ion Batteries. *ACS Sustain. Chem. Eng.* **2025**, *13*, 890–897.
11. Liang, G.; Mo, F.; Ji, X.; et al. Non-metallic charge carriers for aqueous batteries. *Nat. Rev. Mater.* **2021**, *6*, 109–123.
12. Yu, D.; Tian, R.; Du, F. Recent advances in aqueous batteries with nonmetal cations as charge carriers. *Adv. Energy Sustain. Res.* **2022**, *3*, 2100207.
13. Wang, Y.; Kuchena, S.F. Recent progress in aqueous ammonium-ion batteries. *ACS Omega* **2022**, *7*, 33732–33748.
14. Lu, Y.; Wang, T.; Naresh, N.; et al. Pre-doped cations in V_2O_5 for high-performance Zn-ion batteries. *Nano Res. Energy* **2024**, *3*, e9120125.
15. Lu, T.H.; Liu, Q.; He, J.; et al. Ethanediamine Intercalation Induced Hydrogen Bond Network in Vanadium Oxide for Ultralong-Life Aqueous Ammonium Ion Batteries. *Batter. Supercaps* **2025**, *8*, e202400426.
16. Wang, Y. Tailoring Electrodes and Electrolytes in Emerging Aqueous Ammonium-Ion Batteries for Enhanced Performance. In *Electrochemical Society Meeting Abstracts 241*; The Electrochemical Society, Inc.: Pennington, NJ, USA, 2022.

17. Zheng, R.; Li, Y.; Yu, H.; et al. Ammonium ion batteries: Material, electrochemistry and strategy. *Angew. Chem.* **2023**, *135*, e202301629.
18. Uçan, M.; Tekin, B. Toward a Safer and Greener Future: Reliable Aqueous Ammonium-Ion Batteries with $LiMnO_2$ Cathodes. *Bitlis Eren Üniversitesi Fen Bilim. Derg.* **2025**, *14*, 1787–1801.
19. Uçan, M.; Topcu, Y.; Tekin, B. First-Ever Use of $LiMn_2O_4$ Cathode in State-of-the-Art Ammonium-Ion Batteries: Unlocking a New Ametal Charge Carrier. *Erzincan Univ. J. Sci. Technol.* **2025**, *18*, 431–450.
20. Bao, S.-J.; Jia, W.; Lei, C.; et al. Preparation and Electrochemical Capacitor Properties of Novel Birnessite-Type Manganese Dioxide. In *ECS Meeting Abstracts*; IOP Publishing: Jefferson City, MO, USA, 2012; p. 117.
21. Wang, M.; Yagi, S. Layered birnessite MnO_2 with enlarged interlayer spacing for fast Mg-ion storage. *J. Alloys Compd.* **2020**, *820*, 153135.
22. Song, X.; Wang, H.; Li, Z.; et al. A review of MnO_2 composites incorporated with conductive materials for energy storage. *Chem. Rec.* **2022**, *22*, e202200118.
23. Salmani, M.R.M.; Mirkazemi, S.M.; Rezaie, H. The effect of Ni^{2+} and Co^{2+} dopants on the structural, electrical and optical properties of $Sn_{2-x-y}Ni_xCo_yO_{2-z}F_z$ thin films. *Appl. Phys. A* **2025**, *131*, 531.
24. Miao, G.; Wang, Z.; Sun, F.; et al. Modulating the interlayer H^+ migration in MnO_2 via W and K co-doping engineering to high-capacity aqueous zinc-ion batteries. *J. Colloid Interface Sci.* **2025**, *693*, 137636.
25. Wu, Y.; Xu, L.; Zhong, J.; et al. K^+ doping-induced pillaring effect in $Na_3V_2(PO_4)_3$ for enhanced rate performance in sodium-ion batteries. *Chem. Commun.* **2025**, *61*, 13445–13448.
26. Xu, J.-H.; Zhu, Y.-H.; Yang, W.-M.; et al. K doping stabilizes three-dimensional $K_{0.2}Na_{1.3}Mn_{0.5}O_{2-\delta}$ as high-performance cathode for sodium-ion batteries. *Rare Met.* **2024**, *43*, 5030–5038.
27. Yue, Z. Hydrothermal Synthesis of MgAlZnFeCe Hydrotalcite-like Precursors and Their Complex Oxides for Application in FCC De-SO_x. *Wuji Cailiao Xuebao J. Inorg.Mater.* **2009**, *24*, 171–174.
28. Gu, H.; Wang, F.; Chen, S.; et al. Suppressing Jahn-Teller distortion of MnO_2 via B-Ni dual single-atoms integration for methane catalytic combustion. *Nat. Commun.* **2025**, *16*, 1008.
29. Tan, B.; Chen, N.; Huang, L.; et al. Enhanced the electrochemical performance of Ni-doped α-MnO_2 prepared with one-pot process for supercapacitors. *J. Ind. Eng. Chem.* **2025**, *141*, 319–327.
30. Yang, S.; Li, F.; Fu, P.; et al. Nickel-doped δ-MnO_2 abundant in oxygen vacancies as a cathode material for aqueous Zn-ion batteries with superior performance. *Nanoscale* **2025**, *17*, 7423–7433.
31. Raskar, N.D.; Dake, D.V.; Mane, V.A.; et al. Designing reduced graphene oxide decorated Ni doped δ-MnO_2 nanocomposites for supercapacitor applications. *Mater. Sci. Semicond. Process.* **2024**, *178*, 108451.
32. Gou, L.; Li, J.; Liang, K.; et al. Bi-MOF Modulating MnO_2 Deposition Enables Ultra-Stable Cathode-Free Aqueous Zinc-Ion Batteries. *Small* **2023**, *19*, 2208233.
33. Wang, W.; Ren, G.; Wang, M.; et al. A novel composite for energy storage devices: Core–shell MnO_2/polyindole nanotubes supported on reduced graphene oxides. *J. Mater.Sci. Mater. Electron.* **2018**, *29*, 5548–5560.
34. Wang, J.; Gao, X.; Wang, Y.; et al. Robust ring insoluble naphthoquinone derivative cathode with high loading and long cycle life for aqueous zinc organic batteries. *Nano Res. Energy* **2024**, *3*, e9120124.
35. Liu, W.; Qiao, F.; Zhao, J. Tuning electrochemical properties of carbon nanofiber electrodes with selenium heteroatoms for flexible zinc ion capacitors. *Nano Res. Energy* **2024**, *3*, e9120131.